Cite This: ACS Nano 2019, 13, 9655-9663

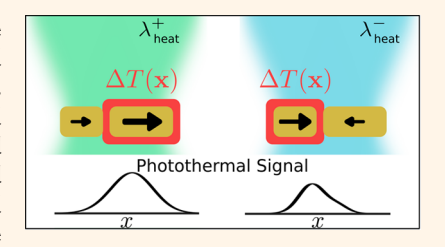
Active Far-Field Control of the Thermal Near-Field via Plasmon Hybridization

Ujjal Bhattacharjee, $^{\dagger,\$,\nabla}$ Claire A. West, $^{\sharp,\nabla}$ Seyyed Ali Hosseini Jebeli, $^{\perp,\nabla}$ Harrison J. Goldwyn, $^{\sharp,0}$ Xiang-Tian Kong, $^{\sharp,0}$ Zhongwei Hu, $^{\sharp,0}$ Elliot K. Beutler, Wei-Shun Chang, Katherine A. Willets, Stephan Link, $^{\sharp,\dagger,\perp,0}$ and David J. Masiello $^{\ast,\sharp,0}$

Supporting Information

Downloaded via UNIV OF WASHINGTON on October 24, 2019 at 04:21:20 (UTC). See https://pubs.acs.org/sharingguidelines for options on how to legitimately share published articles.

ABSTRACT: The ability to control and manipulate temperature at nanoscale dimensions has the potential to impact applications including heat-assisted magnetic recording, photothermal therapies, and temperature-driven reactivity. One challenge with controlling temperature at nanometer dimensions is the need to mitigate heat diffusion, such that the temperature only changes in well-defined nanoscopic regions of the sample. Here we demonstrate the ability to use far-field laser excitation to actively shape the thermal near-field in individual gold nanorod heterodimers by resonantly pumping either the in-phase or out-of-phase hybridized dipole plasmon modes. Using single-particle photothermal heterodyne



imaging, we demonstrate localization bias in the photothermal intensity due to preferential heating of one of the nanorods within the pair. Theoretical modeling and numerical simulation make explicit how the resulting photothermal images encode wavelength-dependent temperature biases between each nanorod within a heterodimer, demonstrating the ability to actively manage the thermal near-field by simply tuning the color of incident light.

KEYWORDS: thermoplasmonics, plasmon hybridization, photothermal imaging, temperature measurements, temperature gradient, nanoscale heating, heterodimer

he remarkable ability of noble metal nanoparticles to convert photon energy to thermal energy has had a significant impact across fields as wide ranging as nanomedicine, ¹⁻³ data storage, ⁴⁻⁷ and clean energy. Underlying the conversion of light to heat is the nonradiative decay of the localized surface plasmon (LSP), a geometryspecific collective oscillation of the free electron gas within a noble metal nanostructure driven by electromagnetic radiation. Over the past decade, significant advances in understanding the nonradiative decay of LSPs has led to the optimization of nanoparticle morphology¹² and assembly^{13,14} as to efficiently capture and convert incident light into heat at the nanoscale.

Modifying the temperature within and around plasmonic nanoparticles relies on managing the production of heat from the decay of LSPs. This process begins within femtoseconds of excitation when LSPs dephase into a nonthermal distribution of so-called "hot" electrons that subsequently relax over picoseconds by electron-electron and electronphonon scattering. 15,16 The resulting temperature is maximized when the particle is excited at the LSP absorption resonance, with a linear increase in temperature as a function of excitation power. If the nanoparticle is embedded in an environment with a low thermal conductivity, the temperature increase will be nearly uniform within the structure and will sharply fall off outside. Thus, highly localized thermal near-fields can be generated at the surface of single plasmonic nanostructures by using far-field optical excitation.

By creating assemblies of nanoparticles, such as dimers and trimers, interparticle plasmon coupling can increase temperatures beyond those found in individual particles. 12,14 The idea of using assemblies of plasmonic nanoparticles is wellestablished in surface-enhanced spectroscopies, in which sizable electromagnetic field enhancements (e.g., "hot spots") can be generated in the gaps between adjacent nanoparticles.¹⁷ However, the regions of strongest field enhancement in nanoparticle assemblies are not correlated with regions of high temperature, 18 as the thermal near-field depends on both the power absorbed by each nanoparticle as well as the local landscape of thermal conductivities, which govern heat diffusion. In fact, the localization of the electric

Received: June 25, 2019 Accepted: July 30, 2019 Published: July 30, 2019

[‡]Department of Chemistry, University of Washington, Seattle, Washington 98195, United States

 $^{^{\}perp}$ Department of Electrical and Computer Engineering, Rice University, Houston, Texas 77005, United States

Department of Chemistry, Temple University, Philadelphia, Pennsylvania 19122, United States

[†]Department of Chemistry, Rice University, Houston, Texas 77005, United States

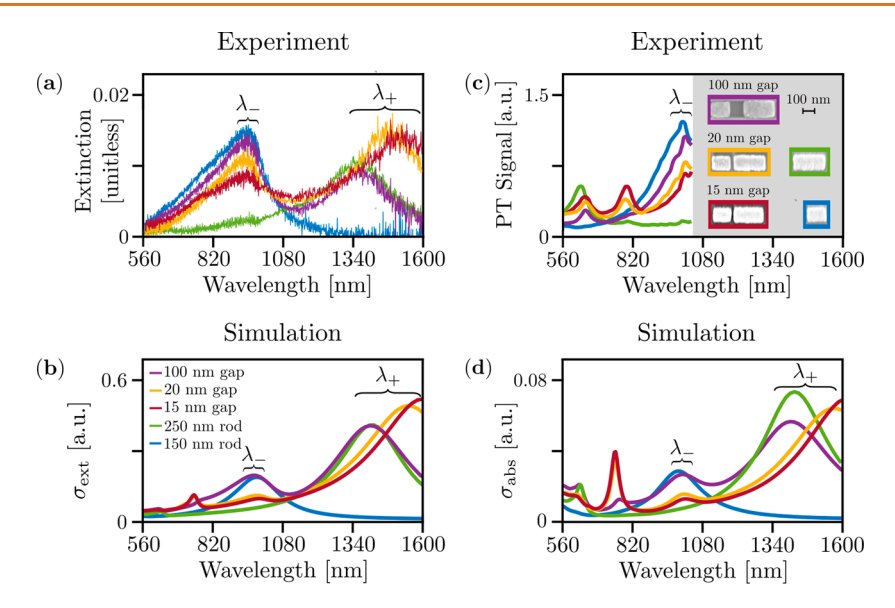


Figure 1. Experimental (a, c) and simulated (b, d) extinction and absorption spectra of individual gold nanorod heterodimers as a function of gap size. The dipole resonances of their basic nanorod components are indicated by the blue and green curves. Scanning electron microscope images of the nanoparticles are shown in (c) with the colored outlines indicating the corresponding spectra. All spectra are for light polarization parallel to the main heterodimer axis; perpendicular polarization is shown in Figure S1. Absorption spectra are limited to 1000 nm due to experimental limitations (see Supporting Information section 1). As nanoparticle separation decreases, the bonding (+) mode increases in amplitude, while the antibonding (-) mode decreases, due to increased hybridization. The bonding mode redshifts with decreasing interparticle gap away from the uncoupled resonance of the 250 nm rod, while the antibonding mode remains almost constant with a small redshift. Worth noting is the correspondence of both modes of the 100 nm gap dimer with the uncoupled rod modes, indicating the weak electromagnetic coupling and weak hybridization across this largest gap heterodimer investigated. Slight differences in relative amplitudes between experiment and simulation are due to small variations in geometry between the nanorods produced by electron-beam lithography and the idealized nanorods used in simulation. Furthermore, the extinction spectra in (a) are stitched together from two detectors, potentially biasing the amplitude of the antibonding mode (see Supporting Information section 1).

field between neighboring particles giving rise to the generation of spatially localized electromagnetic "hot spots" is indicative of plasmon hybridization, which acts to delocalize absorption and optical heating. For example, Baffou and co-workers showed that while electromagnetic "hot spots" are localized in the gap of a nanosphere dimer upon excitation with light polarized along its long axis, the temperature rise due to photothermal heating is uniformly distributed across both nanospheres and is independent of excitation polarization.¹⁹ Thus, while the electric field that penetrates neighboring particles can be exploited to increase the total heat generated (or, oppositely, to minimize unwanted heating in a multiparticle assembly),²¹ it does not intuitively follow that localization of the thermal near-field is achievable in these types of multiparticle assemblies. As a result, photothermal studies on nanoparticle assemblies typically focus on the regime where interparticle spacing is sufficiently large to prevent thermal diffusion between the particles²² or to create assemblies that generate heat over microscale, rather than nanoscale, regions.²

Recent theoretical work, however, has shown that clever design of the geometry of nanoparticle assemblies can create modified thermal profiles, such that heat can be preferentially deposited into specific particles within the assembly using far-field optical excitation.²⁵ This result suggests that it should be possible to use diffraction-limited far-field optical excitation to produce subdiffraction-limited regions of enhanced thermal near-fields within a nanoparticle assembly, thereby creating localized heating at nanoscale dimensions. Put another way, it should be possible to preferentially heat a single nanoparticle

within a multiparticle assembly, even at interparticle spacings where plasmon hybridization occurs. However, no experimental validation of this prediction has yet been made.

In this paper, we demonstrate active light-driven control of the thermal near-field surrounding pairs of hybridized gold nanorods through a combination of single-particle photothermal heterodyne imaging, 26-30 together with coupled optical and heat diffusion modeling of the photothermal signal. By optically pumping either the bonding (λ_+) or antibonding (λ_{-}) dipole LSP resonances of nanofabricated nanorod heterodimers of varying interparticle spacing, we observe spatially asymmetric photothermal images that we correlate to modified local temperature distributions within each individual hybridized nanorod pair. The temperature profiles can be modified by tuning the excitation wavelength, polarization, and position of the excitation field, allowing us to control the thermal near-field using only far-field excitation. Note that unlike in our previous theoretical work where we exploited near-field interferences between multiple normal modes to localize temperature increases, 25 here we bias the temperature between monomers within a single dimer normal mode based only upon the differing optical and thermal polarizabilities of each monomer within the hybridized dimer. Our results establish a strategy for the design of a class of thermal metamaterials capable of controllably directing heat power to precise nanoscopic regions of space, thereby producing thermal profiles of arbitrary shape that depend only upon parameters of the pump laser.³¹

RESULTS AND DISCUSSION

To understand the design challenges introduced by LSP coupling, it is instructive to model the gold nanorod heterodimers as pairs of coupled dipoles. At close proximity, the two independent plasmon dipoles, represented by the generalized coordinates Q_1 and Q_2 , hybridize^{32–34} into the bonding and antibonding normal mode pairs:

$$Q_{+} = \left(\frac{m_{1}}{m_{2}}\right)^{1/4} \cos \theta Q_{1} + \left(\frac{m_{2}}{m_{1}}\right)^{1/4} \sin \theta Q_{2}$$

$$Q_{-} = -\left(\frac{m_{1}}{m_{2}}\right)^{1/4} \sin \theta Q_{1} + \left(\frac{m_{2}}{m_{1}}\right)^{1/4} \cos \theta Q_{2}$$
(1)

with effective mass, m_j (j=1,2), inversely proportional to the polarizability of the $j^{\rm th}$ LSP and rotation angle $\theta=\frac{1}{2}{\rm tan}^{-1}\Big(\frac{2g}{\sqrt{m_1m_2}(\omega_1^2-\omega_2^2)}\Big)$ dictating the degree of mode mixing between isolated nanorod monomers with dipole—dipole coupling strength g and detuning $\omega_1^2-\omega_2^2$. As shown below, asymmetrically increasing the temperature in one of the nanorods relative to the other will require that the Q_1 (or Q_2) contribution is minimized in the hybridized $Q_{+,-}$ modes. This can be accomplished by tuning parameters such as relative nanorod length, material composition, interparticle separation, and angle of illumination. In this paper, we fix the effective mass (or polarizability) ratio with 250 and 150 nm long gold nanorods while varying the coupling g by changing the interparticle spacing.

Figure 1a,c presents single-particle extinction and absorption spectra of individual gold nanorods and individual gold nanorod heterodimers with interparticle gaps of 15, 20, and 100 nm. The absorption measurements were performed in a glycerol environment with the nanorods fabricated on a silica substrate and the pump laser polarized along the heterodimer's long axis. As we are limited to wavelengths below 1000 nm for our current absorption spectroscopy setup, extinction spectra collected in a normal incidence geometry on individual nanostructures complement the spectral characterization of these nanostructures.³⁶ Simulated absorption and extinction spectra are calculated in a glycerol background only as silica and glycerol have similar optical constants in the relevant visible and near-infrared regimes. Simulated extinction and absorption spectra (Figure 1b,d) agree well with the experiments and allow for identification of the hybridized modes. The extinction spectra in Figure 1a,b show the hybridized bonding (+) and antibonding (-)modes of each heterodimer as well as the peak LSP wavelengths of the isolated monomers. Reducing the gap size between the nanorods increases coupling and shifts the bonding resonance to longer wavelengths and higher amplitude. The antibonding mode decreases in amplitude as coupling increases and slightly red shifts due to competition between mode splitting, radiation damping, and the presence of higher-order plasmon modes. Figure 1c shows the spectral decomposition of the photothermal signal (i.e., the absorption spectra) of the three nanorod heterodimers' antibonding modes; the bonding modes seen in the simulated absorption spectra (Figure 1d) are not experimentally characterized due to the aforementioned detection limitations for acquiring absorption spectra. The

resonance peaks between 560 and 820 nm are higher order modes discussed in Figure S6.

Photothermal imaging of each individual heterodimer using excitation wavelengths that span across the dipolar bonding and antibonding modes was performed to map the spectral evolution of the thermal near-field. Unlike the absorption spectrum (Figure 1c), where we are limited spectrally to 1000 nm, photothermal images can be measured up to 1550 nm (see Supporting Information section 1). In the following we will show that the spatial profile of each photothermal image is an indirect measure of the local temperature distribution created when exciting different hybridized plasmon modes and is dependent upon the specific imaging method.

Photothermal heterodyne imaging is a two-laser technique in which the first laser resonantly heats the system at a modulated frequency, thereby increasing the nanorod temperature and, in turn, that of its surrounding local environment. This temperature gain increases the refractive index of the surrounding environment according to

$$n(T(\mathbf{x})) \approx n(T_{R}) + \frac{dn}{dT} \Big|_{T=T_{R}} (T(\mathbf{x}) - T_{R})$$
(2)

where $n(T(\mathbf{x}))$ is the temperature- and space-dependent refractive index and T_R is the initial ambient temperature before optical pumping. A second off-resonant probe beam incident on these regions of increased refractive index scatters differently from the unpumped room temperature system. The photothermal image is created by raster scanning the sample and recording the scattered probe intensity via lock-in detection. Although photothermal imaging is diffractionlimited, a two-beam imaging technique has an inherent resolution advantage, and the nanorod heterodimers fabricated here are sufficiently large to make it possible to spatially resolve differences in the photothermal signal across each individual heterodimer (Figure S2). If the far-field excitation source is able to differentially heat each nanorod within the heterodimer, then we expect a spatial asymmetry in the photothermal image due to spatial variations in the temperature-dependent refractive index of the surroundings.

Indeed, Figure 2 shows different spatial profiles for the photothermal images of the three nanorod heterodimers over a range of pump wavelengths, spanning the dipolar bonding and antibonding mode resonances using a probe beam of 532 nm. Two-dimensional photothermal intensity images for each heterodimer at different pump wavelengths are shown together with one-dimensional line sections taken through the signal maximum. For all three heterodimers, the spatial bias of the photothermal signal intensity (and related temperature profile, as will be shown below) shifts from the 250 nm to the 150 nm nanorod, as the excitation wavelength is tuned from the bonding to the antibonding LSP modes, respectively. This behavior is absent for a heating beam with polarization perpendicular to the nanorod main axis, as mode selective excitation is no longer possible (Figure S3).

While not directly observable, thermal distributions of each heterodimer can be inferred from heat diffusion theory. Steady-state temperature profiles of the bonding and antibonding mode resonances are calculated by numerically solving the steady-state heat diffusion equation $-\nabla \cdot [\kappa - (\mathbf{x})\nabla T(\mathbf{x})] = Q(\mathbf{x})$ sourced by the heat power density $Q(\mathbf{x})$ absorbed from the pump laser, where $\kappa(\mathbf{x})$ and $T(\mathbf{x})$ are the

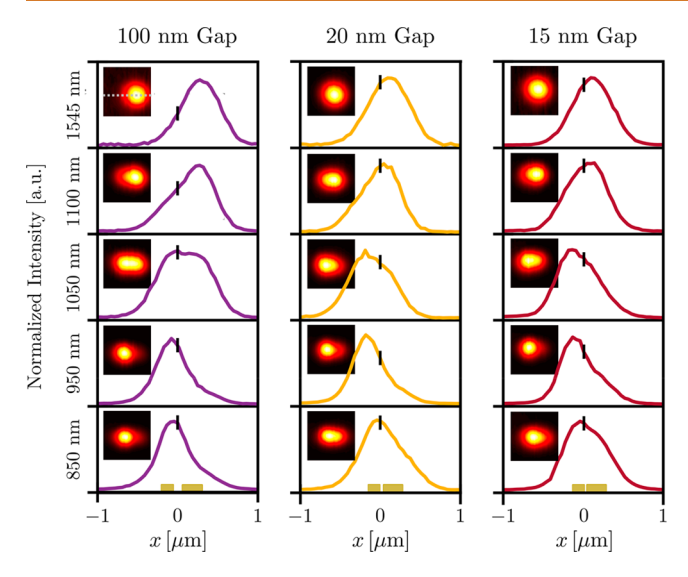


Figure 2. Photothermal images of three nanorod heterodimers of different gap size versus pump wavelength. The pump beam polarization is parallel to the nanorods' long axis, with the nanorods' orientation indicated by the gold bars in the bottom panels. As the wavelength is decreased, the photothermal image maximum moves from the 250 nm nanorod (rightward biasing) to the 150 nm nanorod (leftward biasing). The one-dimensional line sections are the normalized photothermal signal intensity on the horizontal line going through the maximum of each image (dotted line in the first inset), clearly showing how the profile changes shape and position depending on coupling (i.e., gap size) and excitation wavelength. A black line is shown at x = 0 (center of nanoparticle gap) in each panel to guide in observing the transition from rightward to leftward biasing. The wavelengths between bonding and antibonding modes present a region that can be considered nonresonant for the excitation of the heterodimer modes. The response of higher order modes at shorter wavelengths is given in Figure S4. Note that we compare here the photothermal images taken at different wavelengths with their intensities normalized, as we cannot compare the measured relative intensities directly without an independent standard. The standard used for the absorption spectra in Figure 1 was a 35 nm thin gold film that gave insufficient absorption beyond 1000 nm (see Supporting Information section 1). The spatial resolution is obtained by imaging the individual nanorods (Figure S2). It is 600 nm for the longest wavelength and 450 nm for all others, as it is mainly determined by the 532 nm probe beam.

space-dependent thermal conductivity and temperature. The calculation is performed using the thermal discrete-dipole approximation (T-DDA),²⁵ which generalizes the DDA³ concept by allowing each DDA target point to additionally be thermally conductive. In analogy to the familiar DDA, the target is discretized into a collection of thermally polarizable points that are each heated by absorption of light and come into self-consistency with all other points in accordance with Fourier's law of diffusion. Both the infinite background of glycerol and the silica substrate are included in the thermal calculations, the latter by exploiting an analogy to the image effect of electrostatics³⁹ (see Supporting Information section 2). Separate analysis of near-field thermal radiation as a heat transport mechanism shows minimal effects in this system in comparison to diffusion and is therefore omitted from the temperature calculations (see Supporting Information section 2). Additionally, due to the nanometer length scales of the heterodimer and surrounding glycerol, the characteristic

velocity of the glycerol will be very small, making heat transport via convection negligible in comparison to conduction.⁴⁰

Figure 3 displays simulated temperature profiles of the three heterodimers as a Gaussian pump beam is raster scanned across the long axis of each heterodimer. The blue dot indicates the position of the center of the pump beam, where each new beam position excites a different temperature profile. At the bonding modes of all heterodimers, the temperature is highest within the 250 nm rod, with the only difference between each beam position being a change in magnitude of the temperature difference between the 250 and 150 nm rod. This is consistent with the measured photothermal images in the first row of Figure 2 that display rightward biasing at the bonding modes. However, at the antibonding modes for each heterodimer, the position of the Gaussian beam changes the magnitude and sign of the difference in temperature. When the beam is centered on the 250 nm nanorod in each of the three heterodimer gap sizes, the temperature on the 250 nm nanorod is slightly higher than the 150 nm nanorod. Yet, when the beam is centered on the 150 nm nanorod, that nanorod becomes hotter than the 250 nm nanorod. For the 100 nm gap heterodimer, the temperature difference between the two nanorods is greatest here, and in the 20 and 15 nm gap heterodimers, the temperature magnitude is greatest, even though the differences in temperature between the nanorods are similar. By comparing the trends with decreasing gap size, it is clear that the differences in temperature between nanorods are decreasing, indicative of increased thermal coupling caused by the diminishing insulating material (i.e., glycerol) within the gap. This result elucidates the compromise between electromagnetically coupling the nanoparticles to drive stronger hybridization at the expense of heat diffusing between the particles, causing the temperature to become more uniform across the heterodimer. Even so, it is apparent that hybridization enables the ability to tune the thermal profile within and around plasmonic nanoparticles in close proximity despite heat diffusion working in opposition.

To better understand the relationship between the experimental photothermal images and computed temperature profiles, we simulate the photothermal imaging process. As introduced in previous literature, 26-29 the photothermal signal is determined by subtracting the room temperature intensity (I_R , pump beam off) from the hot intensity (I_H , pump beam on), that is, $I^{PT}(x) = I_H(x) - I_R(x)$, to construct simulated point spread functions (PSFs). While the experimental signal is extracted by modulating the pump beam, two separate scattering calculations are performed to simulate the same observable. In the first, the refractive indices of the metal are modified using the temperature profiles shown in Figure 3 based on the optical heat power absorbed by the rastered Gaussian pump laser using a temperature-dependent Drude model.41 We then compute the scattering of a co-scanned Gaussian beam representing the probe beam through these heated points with thermally modified refractive indices acting as a thermal lens. By collecting and integrating the forward scattered light at each beam position (x), we compute an observable proportional to the hot photothermal intensity, $I_{H}(x)$. The intensity of the probe field scattered at room temperature, $I_R(x)$, is calculated in the same manner but instead by using the roomtemperature values $n(\mathbf{x},T) = n(\mathbf{x},T_R)$ for all optical constants.

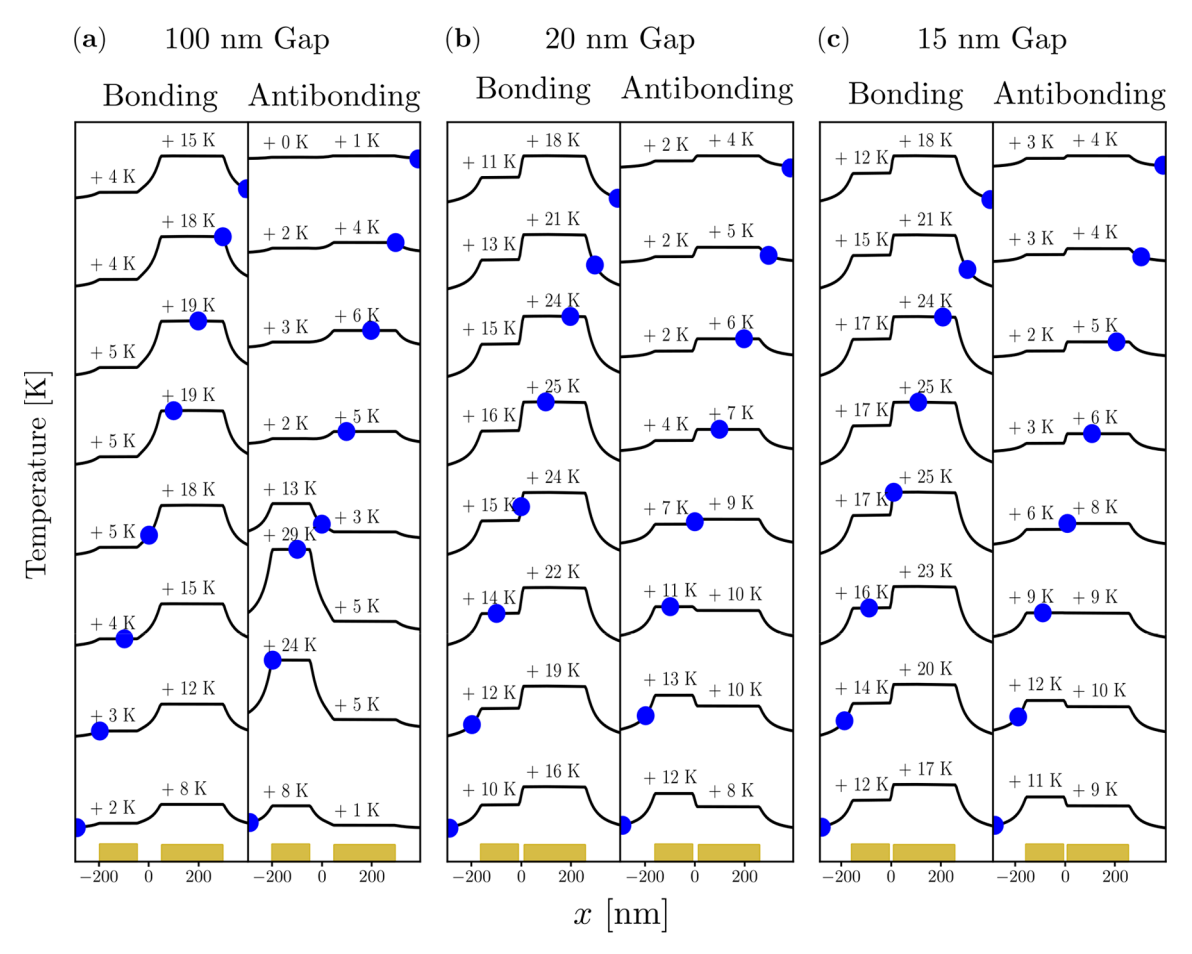


Figure 3. Simulated temperature profiles of the three nanorod heterodimers at their respective bonding and antibonding LSP resonances. The blue dots indicate the centroid of the Gaussian laser profile as the pump beam is raster scanned across the long axis of each heterodimer. The waist of the beam $w = 0.6\lambda/\text{NA}$ is chosen to model the experiment (λ is the bonding/antibonding wavelength, and NA is the experimental numerical aperture) with values that range from $w \approx 480$ to 830 nm. As the beam is raster scanned across each heterodimer, different temperature profiles are created. At the bonding modes of all three gap sizes, the 250 nm rod is hotter than the 150 nm rod regardless of beam position. However, at the antibonding modes, the temperature difference between the two particles is dependent on beam position; the largest magnitude is achieved when the beam is centered on the 150 nm particle, while the sign of the difference changes when the beam is centered on the larger particle. These temperature profiles are used as an input source for the simulated PSFs in Figure 4.

The difference of these calculations represents the measured PSFs of the photothermal signal and can be compared to the experimental images and line sections shown in Figure 2.

Figure 4 displays the simulated photothermal PSFs of each nanorod heterodimer below the corresponding experimental data. Line sections of the PSFs along the symmetry axis of the heterodimers appear in black for all three gap sizes at both dipolar λ_+ and λ_- normal mode resonances. The blue and green curves display the corresponding signal for the isolated nanorods at the same wavelengths. The nanorod locations are represented by the rectangular gold bars with the gap centered at the origin. The isolated monomer PSFs are indicative of the spatial locations of those particles within the heterodimer, and thus comparing the heterodimer PSFs to those of the monomers quantifies the degree of asymmetry as a function of gap size at each hybrid LSP resonance.

Critical to the interpretation of the heterodimer PSF biasing in Figure 4 is an understanding of its relationship to local temperatures. The necessary connection can be elucidated through an idealized analytic model of two dipoles that are electromagnetically and thermally coupled in the near-field and that can scatter light to the far-field. As

detailed in Supporting Information section 3, the dependence of the photothermal images on temperature can be understood under the approximation that each nanorod embedded within its surrounding glycerol environment scatters light approximately as a polarizable point dipole, coupled to the neighboring nanorod dipole through near-field dipole-dipole interactions. The fields scattered by these effective dipoles at room and elevated temperatures are determined by their temperature-dependent polarizabilities $lpha_{\!\scriptscriptstyle i}(T)pprox lpha_{\!\scriptscriptstyle i}^{\,\scriptscriptstyle R}+rac{\mathrm{d}lpha_{\!\scriptscriptstyle i}}{\mathrm{d}T_{\!\scriptscriptstyle i}}(T_{\!\scriptscriptstyle i}-T_{\!\scriptscriptstyle R})$ expanded to first order in variation with temperature of the *i*th nanorod (i = 1, 2). Here, α_i^R is the room-temperature polarizability, and $T_i \equiv$ $T(\mathbf{x}_i)$ is the temperature of the *i*th nanorod and the surrounding heated glycerol. Within this idealized model, the photothermal image can be understood as the superposition of two airy disk PSFs representing the near diffraction-limited image of each nanorod's scattered field. These scattered fields also interfere, effectively blurring the superposition of the two PSFs. As shown in Supporting Information section 3, by including both superposition and

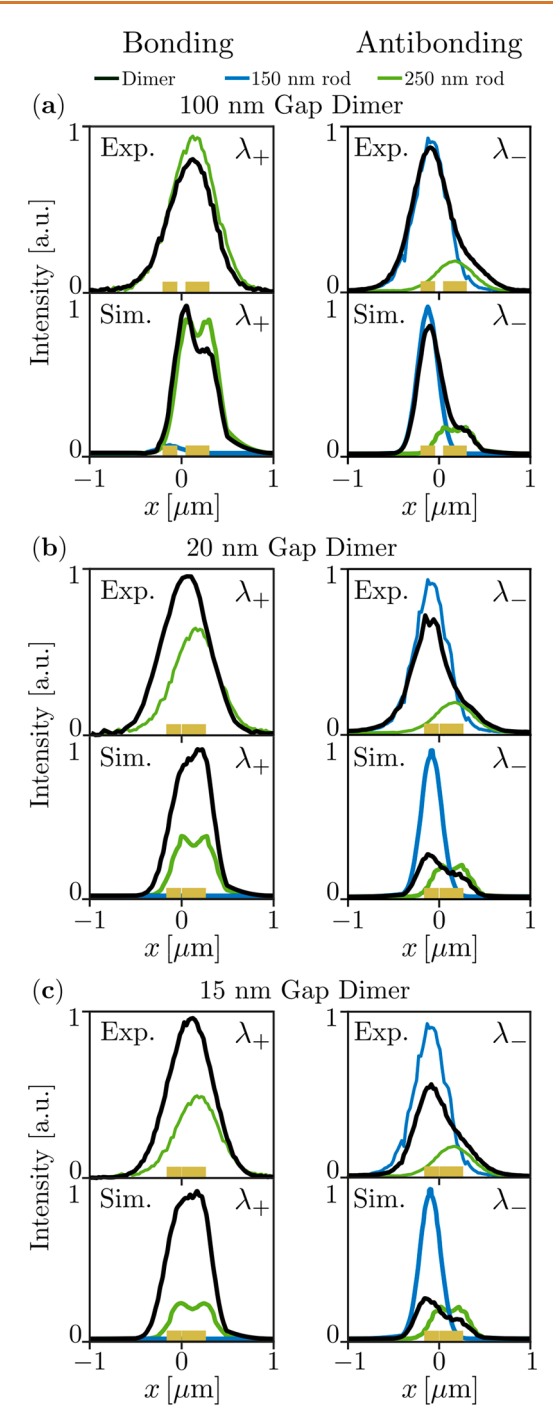


Figure 4. Excitation wavelength-dependent biasing of the photothermal image. Experimental and simulated line sections of PSFs of the three nanorod heterodimers at each gap size are shown for excitation at the bonding λ_+ mode (1545 nm) and the antibonding λ_{-} mode (950 nm). Their respective isolated monomers are also given. Nanorod positions are indicated by the gold bars. Mapping of experimental PSFs and the actual nanostructure positions was achieved with fiduciary markers (Figure S5). Furthermore, the photothermal intensities are scaled to the measured signal allowing for a direct comparison of magnitudes. For all heterodimers, experimental and simulated PSF line sections indicate rightward biasing at the bonding λ_{+} mode and leftward biasing at the antibonding λ_{-} mode. Additionally for the 20 and 15 nm gap PSFs, the magnitudes of the heterodimer PSFs (black) are larger at the bonding mode compared to the isolated 250 nm nanorod (green), and, oppositely, the magnitude of the heterodimer at the antibonding

Figure 4. continued

mode is smaller than the isolated 150 nm nanorod (blue). The double-lobed feature of the simulated 250 nm monomer PSF results from increased scattering at the nanorod ends and is not visible in the experiment due to resolution. Experimentally, no PSFs can be recorded for the isolated 150 nm nanorods at the bonding mode because the absorption is too weak (blue). Note that in experiment, the excitation wavelengths are fixed, and therefore a direct comparison of the PSF location and intensity between the different nanostructures is possible. Simulations model this scenario.

interference effects, the dependence of the photothermal image on the temperature of each nanorod can be written as

$$\frac{I^{\text{PT}}(\mathbf{x})}{I_{\text{inc}}} = \frac{8\pi k^4}{3A_{\text{PD}}} \left(2\text{Re} \left| \alpha_1^{\text{R}^*} \frac{d\alpha_1}{dT_1} \right|_{T_R} (T_1 - T_R) \right)
f_{\text{PSF}}(\mathbf{x} - \mathbf{x}_1) + 2\text{Re} \left[\alpha_2^{\text{R}^*} \frac{d\alpha_2}{dT_2} \right|_{T_R} (T_2 - T_R) \right]
f_{\text{PSF}}(\mathbf{x} - \mathbf{x}_2) + 2\text{Re} \left[\alpha_2^{\text{R}^*} \frac{d\alpha_1}{dT_1} \right|_{T_R} (T_1 - T_R)
+ \alpha_1^{\text{R}^*} \frac{d\alpha_2}{dT_2} \right|_{T_R} (T_2 - T_R) \left| f_{\text{IF}}(\mathbf{x} - \mathbf{x}_1, \mathbf{x} - \mathbf{x}_2) \right|$$
(3)

assuming minimal coupling between the nanorods from the probe laser. In this expression, $I_{\rm inc}$ is the incident probe intensity and $A_{\rm PD}$ is the area of the photodetector. Each PSF $(f_{\rm PSF})$ scales linearly with temperature (T_i) , but also with the room temperature polarizability of the ith nanorod. The scaling of each PSF and interference PSF $(f_{\rm IF})$ with temperature $\alpha_i^{\rm R^*} \frac{{\rm d}\alpha_i}{{\rm d}T_i}\bigg|_{T_{\rm R}}$ differs between the two nanorods and

complicates the relationship between local temperature and photothermal image magnitude. Also, because this image is generated by rastering both the pump and probe lasers across positions \mathbf{x} , it is important to note that the nanorod temperatures $T_{1,2}$ are implicit functions of the beam position \mathbf{x} as demonstrated in Figure 3. Nonetheless, it is evident that the photothermal image biases in the direction of increased temperature and increased polarizability, meaning that asymmetry in the PSF is positively correlated with nanoscale asymmetry in temperature and nanorod polarizability.

Equipped with the intuition gained from eq 3 to interpret the local temperature dependence of the photothermal PSFs, Figure 4 displays the experimental PSFs above those computed from the simulated temperatures in Figure 3. The bonding mode PSFs of the 100, 20, and 15 nm gap heterodimers in experiment and simulation exhibit strong localization to the longer nanorod, as seen by comparing the heterodimer PSFs (black) to the isolated 250 nm monomer PSFs (green.) The 100, 20, and 15 nm gap heterodimer PSFs at the antibonding wavelength are oppositely localized over the smaller 150 nm nanorod, yet retain noticeable shoulders over the 250 nm nanorod in both experiment and simulation. This lesser degree of photothermal localization compared to

the bonding mode is due to non-negligible photothermal signal originating from the 250 nm nanorod even though it is minimally heated by excitation at the antibonding wavelength, as well as the smaller temperature differences between the nanorods compared to the large differences achieved at the bonding mode resonance.

CONCLUSIONS

Controlling the distribution of heat and temperature at nanoscale dimensions using far-field optical excitation is challenging due to the counteracting effects of the diffraction limit of light and the diffusion of heat. Here we have shown the surprising ability to overcome thermal diffusion and create nanolocalized distributions of increased temperature in hybridized plasmonic nanoparticle clusters that are actively tunable from the far-field simply by changing the wavelength of the pump field. Our approach relies upon asymmetries in the spatial distribution of in-phase and out-of-phase plasmonic normal modes in individual nanofabricated gold nanorod heterodimers of varying inter-rod spacing. Using single-particle photothermal heterodyne imaging, we observed spatial biasing in the photothermal PSFs measured at each normal mode resonance and correlated these biases to inhomogeneities of the thermal near-field using analytical models and numerical simulations of the coupled optical and thermal fields. Taken together, this closely integrated experimental and theoretical work demonstrates the ability to actively manipulate the thermal near-field and points to future generalizations involving more complex nanoparticle clusters to create arbitrarily tunable thermal profiles below the diffraction limit. Even larger temperature biasing can be achieved for plane wave excitation where the illumination is larger than the coupled nanostructure, as shown through simulations in Figure S8. This case will be the subject of future combined experimental and theoretical studies.

METHODS

Experimental. In the photothermal heterodyne imaging measurements, the probe laser was a 532 nm diode laser (Coherent OBIS), and the pump laser (Fianium WhiteLase) wavelength was tuned from 500 nm -1550 nm. The pump beam was modulated at a frequency of 30 kHz. The sample was placed in a confocal microscope with a 63× oil immersion objective with a NA = 0.7 for spectra and NA=1.4 for imaging to focus the laser beams onto the sample. A 40× air objective with a NA = 0.6 collected the scattered probe light in a transmission geometry. The signal generated by the scattered light was directed to a lock-in amplifier with an integration time of 30 ms and a sensitivity of 3 mV for all measurements. The pump power was 600 μ W at 800 nm, and the probe power was 1.1 mW. To obtain photothermal contrast images, the pump wavelength was held constant, while the sample was moved using a piezo scanning stage.

Theoretical. The computational approach for obtaining confocal photothermal images used DDSCAT 7.3, modified to account for a Gaussian beam excitation source. The calculations were performed on gold heterodimers using a temperature-dependent Drude model with 5 nm dipole spacing in a uniform infinite glycerol background (n = 1.473) at the wavelength corresponding to each normal mode. The resulting electric field and polarization information within the nanorods were used as inputs to a version of T-DDA²⁵ which includes a semi-infinite silica ($\kappa = 1.38 \text{ W/m K}$) substrate (see Supporting Information section 2.2). The temperatures of each nanorod were then used to modify the dielectric data of gold for a second scattering calculation, performed at an off-resonant probe wavelength of 615 nm. The total intensity of the

forward scattered light from this second scattering calculation at a single Gaussian probe beam position, x_i , is $I_{\rm H}(x_i)$. To obtain the entire photothermal signal, the room-temperature intensity, $I_{\rm R}(x_i)$, found by calculating the scattering from the room-temperature nanorods at a probe wavelength of 615 nm, was subtracted from $I_{\rm H}(x_i)$. Lastly, to obtain each position-dependent line-section, the entire procedure was carried out over a range of co-scanned excitation and probe beam positions that spanned the length of the dimer system.

ASSOCIATED CONTENT

Supporting Information

The Supporting Information is available free of charge on the ACS Publications website at DOI: 10.1021/acsnano.9b04968.

Additional information includes the electron beam lithography fabrication of the gold heterodimers (S1.1) and the experimental procedure for single particle extinction (S1.2), absorption (S1.3), and scattering measurements (S1.4). A detailed representation of the controls and additional photothermal biasing experiments are included (Figures S1–S5). Simulated plane wave (wide-field) heat power density maps (Figure S7) and temperature maps (Figure S8) are also included to contrast the Gaussian beam (confocal) sourced results presented in the main text. A justification for steady-state heat diffusion temperature calculations are provided in (S2.1–S2.3). Lastly, an in-depth model of photothermal imaging and a derivation of eq 3 are presented in S3 (PDF)

AUTHOR INFORMATION

Corresponding Authors

*E-mail: kwillets@temple.edu. *E-mail: slink@rice.edu. *E-mail: masiello@uw.edu.

ORCID

Harrison J. Goldwyn: 0000-0002-7184-2120 Xiang-Tian Kong: 0000-0002-8554-0369 Zhongwei Hu: 0000-0002-2783-7981 Wei-Shun Chang: 0000-0002-0251-4449 Katherine A. Willets: 0000-0002-1417-4656 Stephan Link: 0000-0002-4781-930X David J. Masiello: 0000-0002-1187-0920

Present Addresses

§Department of Chemistry, IIEST Shibpur, West Bengal 711103, India

*Department of Chemistry and Biochemistry, University of Massachusetts Dartmouth, North Dartmouth, Massachusetts 02747, United States

Author Contributions

VThese authors contributed equally.

Notes

The authors declare no competing financial interest.

ACKNOWLEDGMENTS

This work was supported by the U.S. National Science Foundation under grant nos. NSF CHE-1727092 and CHE-1664684 (D.J.M.), CHE-1727122 (S.L.), and CHE-1728340 (K.A.W.). S.L. also acknowledges support from the Robert A. Welch Foundation (grant no. C-1664). This work was facilitated through the use of advanced computational,

storage, and networking infrastructure provided by the Hyak supercomputer system at the University of Washington.

REFERENCES

- (1) Sanchez-Rodriguez, S. P.; Sauer, J. P.; Stanley, S. A.; Qian, X.; Gottesdiener, A.; Friedman, J. M.; Dordick, J. S. Plasmonic Activation of Gold Nanorods for Remote Stimulation of Calcium Signaling and Protein Expression in Hek 293t Cells. *Biotechnol. Bioeng.* 2016, 113, 2228–2240.
- (2) Caterina, M. J.; Schumacher, M. A.; Tominaga, M.; Rosen, T. A.; Levine, J. D.; Julius, D. The Capsaicin Receptor: A Heat-Activated Ion Channel in the Pain Pathway. *Nature* **1997**, 389, 816–824.
- (3) DeFalco, J.; Tomishima, M.; Liu, H.; Zhao, C.; Cai, X.; Marth, J. D.; Enquist, L.; Friedman, J. M. Virus-Assisted Mapping of Neural Inputs to a Feeding Center in the Hypothalamus. *Science* **2001**, *291*, 2608–2613.
- (4) Ghoreyshi, A.; Victora, R. Optical Modeling of Media for Heat Assisted Magnetic Recording. *Appl. Phys. Lett.* **2016**, *108*, 092401.
- (5) Xu, H.; Hajisalem, G.; Steeves, G. M.; Gordon, R.; Choi, B. C. Nanorod Surface Plasmon Enhancement of Laser-Induced Ultrafast Demagnetization. *Sci. Rep.* **2015**, *5*, 15933.
- (6) Ji, R.; Xu, B.; Cen, Z.; Ying, J. F.; Toh, Y. T. Thermal Effects on Transducer Material for Heat Assisted Magnetic Recording Application. J. Appl. Phys. 2015, 117, 17A918.
- (7) Zhou, N.; Xu, X.; Hammack, A. T.; Stipe, B. C.; Gao, K.; Scholz, W.; Gage, E. C. Plasmonic Near-Field Transducer for Heat-Assisted Magnetic Recording. *Nanophotonics* **2014**, *3*, 141–155.
- (8) Baffou, G.; Polleux, J.; Rigneault, H.; Monneret, S. Super-Heating and Micro-Bubble Generation around Plasmonic Nanoparticles under Cw Illumination. *J. Phys. Chem. C* **2014**, *118*, 4890–4898.
- (9) Hogan, N. J.; Urban, A. S.; Ayala-Orozco, C.; Pimpinelli, A.; Nordlander, P.; Halas, N. J. Nanoparticles Heat through Light Localization. *Nano Lett.* **2014**, *14*, 4640–4645.
- (10) Neumann, O.; Urban, A. S.; Day, J.; Lal, S.; Nordlander, P.; Halas, N. J. Solar Vapor Generation Enabled by Nanoparticles. *ACS Nano* **2013**, *7*, 42–49.
- (11) Fang, Z.; Zhen, Y.-R.; Neumann, O.; Polman, A.; García de Abajo, F. J.; Nordlander, P.; Halas, N. J. Evolution of Light-Induced Vapor Generation at a Liquid-Immersed Metallic Nanoparticle. *Nano Lett.* **2013**, *13*, 1736–1742.
- (12) Baffou, G.; Quidant, R.; García de Abajo, F. J. Nanoscale Control of Optical Heating in Complex Plasmonic Systems. *ACS Nano* **2010**, *4*, 709–716.
- (13) Baffou, G.; Quidant, R. Thermo-Plasmonics: Using Metallic Nanostructures as Nano-Sources of Heat. *Laser Photonics Rev.* **2013**, 7, 171–187.
- (14) Khosravi Khorashad, L.; Besteiro, L. V.; Wang, Z.; Valentine, J.; Govorov, A. O. Localization of Excess Temperature Using Plasmonic Hot Spots in Metal Nanostructures: Combining Nano-Optical Antennas with the Fano Effect. *J. Phys. Chem. C* **2016**, 120, 13215–13226.
- (15) Hartland, G. V. Optical Studies of Dynamics in Noble Metal Nanostructures. *Chem. Rev.* **2011**, *111*, 3858–3887.
- (16) Yu, Y.; Wijesekara, K. D.; Xi, X.; Willets, K. A. Quantifying Wavelength-Dependent Plasmonic Hot Carrier Energy Distributions at Metal/Semiconductor Interfaces. ACS Nano 2019, 13, 3629—3637.
- (17) Camden, J. P.; Dieringer, J. A.; Wang, Y.; Masiello, D. J.; Marks, L. D.; Schatz, G. C.; Van Duyne, R. P. Probing the Structure of Single-Molecule Surface-Enhanced Raman Scattering Hot Spots. *J. Am. Chem. Soc.* **2008**, *130*, 12616–12617.
- (18) Baffou, G.; Girard, C.; Quidant, R. Mapping Heat Origin in Plasmonic Structures. *Phys. Rev. Lett.* **2010**, *104*, 136805.
- (19) Metwally, K.; Mensah, S.; Baffou, G. Isosbestic Thermoplasmonic Nanostructures. ACS Photonics 2017, 4, 1544–1551.

(20) Coppens, Z. J.; Li, W.; Walker, D. G.; Valentine, J. G. Probing and Controlling Photothermal Heat Generation in Plasmonic Nanostructures. *Nano Lett.* **2013**, *13*, 1023–1028.

- (21) Albella, P.; Alcaraz de la Osa, R.; Moreno, F.; Maier, S. A. Electric and Magnetic Field Enhancement with Ultralow Heat Radiation Dielectric Nanoantennas: Considerations for Surface-Enhanced Spectroscopies. *ACS Photonics* **2014**, *1*, 524–529.
- (22) Baffou, G.; Berto, P.; Bermúdez Ureña, E.; Quidant, R.; Monneret, S.; Polleux, J.; Rigneault, H. Photoinduced Heating of Nanoparticle Arrays. ACS Nano 2013, 7, 6478–6488.
- (23) Shimada, R.; Sakai, H.; Yamamoto, J.; Watanabe, H. Creation of Large, Periodic Temperature Gradient *Via* Plasmonic Heating from Mesoscopic Planar Lattice of Metal Domains. *Int. J. Therm. Sci.* **2017**, *118*, 247–258.
- (24) Yan, X.; Liu, G.; Xu, J.; Wang, S. Plasmon Heating of One-Dimensional Gold Nanoparticle Chains. *Sol. Energy* **2018**, *173*, 665–674.
- (25) Baldwin, C. L.; Bigelow, N. W.; Masiello, D. J. Thermal Signatures of Plasmonic Fano Interferences: Toward the Achievement of Nanolocalized Temperature Manipulation. *J. Phys. Chem. Lett.* **2014**, *5*, 1347–1354.
- (26) Berciaud, S.; Cognet, L.; Blab, G. A.; Lounis, B. Photothermal Heterodyne Imaging of Individual Nonfluorescent Nanoclusters and Nanocrystals. *Phys. Rev. Lett.* **2004**, 93, 257402.
- (27) Selmke, M.; Braun, M.; Cichos, F. Gaussian Beam Photothermal Single Particle Microscopy. *J. Opt. Soc. Am. A* **2012**, 29, 2237–2241.
- (28) Cognet, L.; Tardin, C.; Boyer, D.; Choquet, D.; Tamarat, P.; Lounis, B. Single Metallic Nanoparticle Imaging for Protein Detection in Cells. *Proc. Natl. Acad. Sci. U. S. A.* **2003**, *100*, 11350–11355.
- (29) Gaiduk, A.; Ruijgrok, P. V.; Yorulmaz, M.; Orrit, M. Detection Limits in Photothermal Microscopy. *Chem. Sci.* **2010**, *1*, 343–350.
- (30) Yorulmaz, M.; Nizzero, S.; Hoggard, A.; Wang, L.-Y.; Cai, Y.-Y.; Su, M.-N.; Chang, W.-S.; Link, S. Single-Particle Absorption Spectroscopy by Photothermal Contrast. *Nano Lett.* **2015**, *15*, 3041–3047.
- (31) Fang, Y.; Chang, W.-S.; Willingham, B.; Swanglap, P.; Dominguez-Medina, S.; Link, S. Plasmon Emission Quantum Yield of Single Gold Nanorods as a Function of Aspect Ratio. *ACS Nano* **2012**, *6*, 7177–7184.
- (32) Quillin, S. C.; Cherqui, C.; Montoni, N. P.; Li, G.; Camden, J. P.; Masiello, D. J. Imaging Plasmon Hybridization in Metal Nanoparticle Aggregates with Electron Energy-Loss Spectroscopy. *J. Phys. Chem. C* **2016**, *120*, 20852–20859.
- (33) Cherqui, C.; Bigelow, N. W.; Vaschillo, A.; Goldwyn, H.; Masiello, D. J. Combined Tight-Binding and Numerical Electrodynamics Understanding of the STEM-EELS Magneto-Optical Responses of Aromatic Plasmon-Supporting Metal Oligomers. *ACS Photonics* **2014**, *1*, 1013–1024.
- (34) Prodan, E.; Radloff, C.; Halas, N. J.; Nordlander, P. A Hybridization Model for the Plasmon Response of Complex Nanostructures. *Science* **2003**, *302*, 419–422.
- (35) Yorulmaz, M.; Hoggard, A.; Zhao, H.; Wen, F.; Chang, W.-S.; Halas, N. J.; Nordlander, P.; Link, S. Absorption Spectroscopy of an Individual Fano Cluster. *Nano Lett.* **2016**, *16*, 6497–6503.
- (36) Slaughter, L. S.; Chang, W.-S.; Swanglap, P.; Tcherniak, A.; Khanal, B. P.; Zubarev, E. R.; Link, S. Single-Particle Spectroscopy of Gold Nanorods Beyond the Quasi-Static Limit: Varying the Width at Constant Aspect Ratio. *J. Phys. Chem. C* **2010**, *114*, 4934–4938.
- (37) Draine, B. T.; Flatau, P. J. Discrete-Dipole Approximation for Scattering Calculations. *J. Opt. Soc. Am. A* **1994**, *11*, 1491–1499.
- (38) Purcell, E. M.; Pennypacker, C. R. Scattering and Absorption of Light by Nonspherical Dielectric Grains. *Astrophys. J.* **1973**, *186*, 705–714.
- (39) Jackson, J. Classical Electrodynamics, 3rd ed.; Wiley, New York, 1999; pp 57-60.

(40) Donner, J. S.; Baffou, G.; McCloskey, D.; Quidant, R. Plasmon-Assisted Optofluidics. *ACS Nano* **2011**, *5*, 5457–5462. (41) Reddy, H.; Guler, U.; Kildishev, A. V.; Boltasseva, A.; Shalaev, V. M. Temperature-Dependent Optical Properties of Gold Thin Films. *Opt. Mater. Express* **2016**, *6*, 2776–2802.